

Dynamic Competition Between Orbital and Exchange Interactions Selectively Localizes Electrons and Holes Through Polarons

Jocelyn L. Mendes¹, Hyun Jun Shin², Jae Yeon Seo², Nara Lee², Young Jai Choi², Joel B. Varley³, and Scott K. Cushing^{1*}

¹ Division of Chemistry and Chemical Engineering, California Institute of Technology, Pasadena, California 91125, United States

² Department of Physics, Yonsei University, Seoul, 03722, Republic of Korea

³ Lawrence Livermore National Laboratory, Livermore, California 94550, United States

*Correspondence and requests for materials should be addressed to S.K.C. (email: scushing@caltech.edu)

Abstract

Controlling the effects of photoexcited polarons in transition metal oxides can enable the long timescale charge separation necessary for renewable energy applications as well as controlling new quantum phases through dynamically tunable electron-phonon coupling. In previously studied transition metal oxides, polaron formation is facilitated by a photoexcited ligand-to-metal charge transfer (LMCT). When the polaron is formed, oxygen atoms move away from iron centers, which increases carrier localization at the metal center and decreases charge hopping. Studies of yttrium iron garnet and erbium iron oxide have suggested that strong electron and spin correlations can modulate photoexcited polaron formation. To understand the interplay between strong spin and electronic correlations in highly polar materials, we studied gadolinium iron oxide (GdFeO_3), which selectively forms photoexcited polarons through an Fe-O-Fe superexchange interaction. Excitation-wavelength-dependent transient extreme ultraviolet (XUV) spectroscopy selectively excites LMCT and metal-to-metal charge transfer transitions (MMCT). The LMCT transition suppresses photoexcited polaron formation due to dominant Hubbard interactions, while MMCT transitions result in photoexcited polaron formation within $\sim 373 \pm 137$ fs due to enhanced superexchange interactions. Ab initio theory demonstrates that both electron and hole polarons localize on iron centers following MMCT. In addition to understanding how strong electronic and spin correlations can control strong electron-phonon coupling, these experiments separately measure electron and hole polaron interactions on neighboring metal centers for the first time, providing insight into a large range of charge-transfer and Mott-Hubbard insulators.

Introduction

Polaron formation in transition metal oxide materials has been widely explored for its effects on ground state transport in correlated materials and solar energy processes like photocatalysis.¹⁻⁵ In highly polar materials, the coupling of photoexcited charge carriers to phonons in the lattice localizes carriers in the form of polarons.⁶ Parameters to dynamically control laser-driven strong electron-phonon coupling is an ongoing search. Understanding and controlling the underlying physics that determines the formation of polarons in materials could provide meaningful

improvements to a wide range of material classes, from organic electronics to solar energy systems and exotic quantum phases.^{7,8}

Hematite (α -Fe₂O₃) and other iron oxides have been extensively explored for their photoexcited polaron formation dynamics.^{9–12} Most of these materials are charge-transfer insulators, where the valence band maximum (VBM) is dominated by O 2p orbitals, and the conduction band minimum (CBM) is dominated by metal 3d orbitals. An above-band gap photoexcitation induces a ligand-to-metal charge transfer (LMCT) transition from oxygen to the metal center. The electronic structures of metal oxides also span intermediate and Mott-Hubbard insulators, where the VBM is dominated by either mixed O/metal orbitals or entirely metal orbitals, respectively. These differing electronic structures pose a unique route for modulation of carrier localization by polaron formation following photoexcitation.

Almost uniformly across iron oxides, photoexcited small polaron formation occurs within a few hundred femtoseconds of the charge transfer transition.^{10,13,14} A subsequent expansion of Fe-O bond lengths and localization of electron density on polaronic Fe sites has been measured using a variety of X-ray spectroscopies. Recent work exploring the tunability of polaronic properties has been demonstrated using structural distortions and strong electron and spin correlations. For example, rare-earth orthoferrite ErFeO₃ was found to have weaker polaronic binding energies because the polaron formation rate was slowed by strong electronic correlations.¹² Additional work comparing hematite and Y₃Fe₅O₁₂ (YIG) finds that strong spin selective dynamics reduce polaron formation in YIG and increase its photocatalytic efficiency by an order of magnitude with respect to hematite.¹⁵ Transient XUV and X-ray spectroscopies, however, have yet to be applied to the simultaneous measurement of electron and hole polarons in intermediate and Mott-Hubbard insulating iron oxides.

Here, we employ excitation-wavelength-dependent transient extreme ultraviolet (XUV) reflection spectroscopy to explore the relation between superexchange and Hubbard interactions in influencing strong carrier localization through polarons in single-crystal rare-earth orthoferrite GdFeO₃. This intermediate insulator (mixed O 2p/Fe 3d VBM) is a model material system for many perovskite Mott-Hubbard insulators due to its crystal structure.^{16,17} It is an ideal system for studying carrier localization because of the coexistence of charge transfer polarons and metal-metal polarons following photoexcitation. GdFeO₃ and other rare-earth orthoferrites have been explored as candidates for photoelectrochemical oxygen reduction and evolution, as well as magneto-optical and spintronic applications due to their demonstrated multiferroicity.^{18,19} Through transient XUV spectroscopy, we find that LMCT from O 2p to Fe 3d orbitals results in the suppression of photoexcited polaron formation, while a metal-to-metal charge transfer (MMCT) induces photoexcited polaron formation despite the LMCT being higher in energy. The MMCT enables polarons by superexchange across an Fe-O-Fe bond, resulting in hole and electron polarons localized on neighboring iron centers. Polaron formation and superexchange is suppressed following a higher energy LMCT due to the dominance of on-site Coulomb repulsion (U) in higher energy Fe d and Gd f dominated bands. Ab initio density functional theory (DFT)

and the Bethe-Salpeter equation (BSE) simulate the photoexcited XUV dynamics. Polaron-induced lattice distortions and charge localization within a defect supercell approach were assessed with different levels of electronic structure theory, ranging from DFT incorporating on-site Hubbard U parameters with variational polaron self-interaction-corrected (pSIC) total-energy functional models to hybrid functionals with different fractions of exact-exchange. The results provide new insight into tuning polaronic properties via strong electronic and spin correlations for transition metal oxide materials, particularly identifying superexchange interactions as a new dynamical carrier localization and polaron design parameter.

Results and Discussion

GdFeO₃ has an orthorhombic symmetry in the $Pbnm$ space group, as shown in Figure 1A.¹⁷ The FeO₆ octahedra are strained due to the large rare-earth atom in the crystal structure, resulting in a 154° Fe-O-Fe bond angle.²⁰ Strong electron correlations introduced by both the Fe d and Gd f orbitals enable a mixed Fe d /O p band at the VBM and a metal d band at the CBM as shown in Figure 1B. This contrasts with previously measured iron oxides whose density of states follows a charge-transfer insulating structure where the VBM is dominated by O p orbitals.^{10,21} DFT+ U is used to accurately describe the extent of carrier localization and on-site repulsion in GdFeO₃.¹⁷ Magnetization studies of GdFeO₃ have demonstrated that it is a canted, G-type antiferromagnet below its Néel temperature (T_N) of ~650 K, resulting in a weak ferromagnetism due to the Dzyaloshinskii-Moriya (DM) interaction.²²⁻²⁴ The Fe³⁺ ions in the GdFeO₃ take a high-spin electronic configuration in their ground state.²⁵

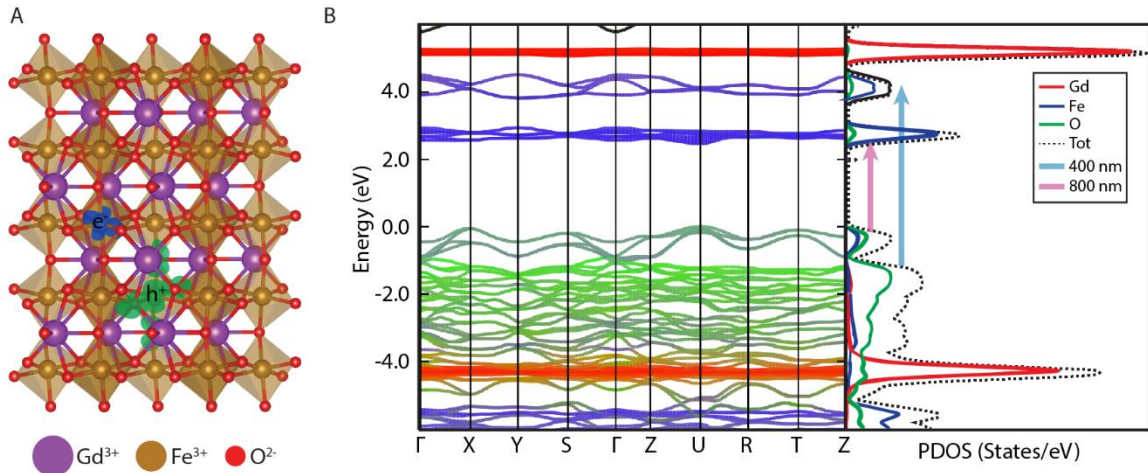


Figure 1. (A) GdFeO₃ crystal structure with electron (blue) and hole (yellow) polaron charge densities as calculated with exchange correlation functionals that correct for self-interaction errors, referred to as defect supercell calculations. The electron and hole polarons are both predicted to be centered on iron atoms. (B) Calculated electronic band structure and projected density of states (PDOS) with the HSE06 hybrid functional with 15% exact exchange for the studied AFM ground state, including tentative assignments of band transitions associated with the 800 nm (pink arrow) and 400 nm (blue arrow) excitations that lead to the polaron formation. The bandgap is overestimated due to deficiencies associated with DFT of transition metals, but the band structure and contributions of relative orbitals is preserved. The excitation arrows are adjusted accordingly to showcase the transition densities expected based upon the experimentally measured band gap.

Figure 1B shows the two photoexcitation pathways used in the excitation-wavelength-dependent XUV measurements. In the case of the 400 nm (3.1 eV) photoexcitation, carriers are excited from lower lying valence bands that are dominated by O p orbitals into higher energy Fe d and Gd f orbital dominated conduction bands. Photoexcitation with 400 nm light follows a LMCT mechanism. The lower energy 800 nm (1.55 eV) photoexcitation induces transitions from the VBM, which are mixed in O p and Fe d orbital character, into lower energy conduction bands dominated by Fe d orbitals. The mixed nature of the VBM in GdFeO₃ poses an opportunity for both MMCT and LMCT to occur following 800 nm photoexcitation.²⁶ These excitation energies provide different possible pathways for polaron formation.

XUV spectroscopy has been employed extensively for measurement of photoexcited polaron formation dynamics because it can evaluate ultrafast, element-specific electronic-structural dynamics.^{9,10,14} Spectrally, polaron formation in iron oxide materials has been characterized in the XUV as a shift to higher energies at the Fe M_{2,3} edge. As carriers localize on the iron center, more energy is required to induce the core-to-valence 3p to 3d transition at the iron site. This has held for charge-transfer polarons across Fe-O materials with dynamics that agree well with transient X-ray diffraction and ultrafast optical techniques.^{27,28}

Transient XUV reflectivity at the Fe M_{2,3} edge of GdFeO₃ pumped with the 800 nm (1.5 eV) and 400 nm (3.1 eV) photoexcitation is shown in Figure 2A and B, respectively. In the 800 nm and 400 nm pumped transient XUV reflectivity spectra, the Fe M_{2,3} edge is characterized immediately after photoexcitation by a negative absorption feature (blue) centered around 54 eV. This spectral feature can be described by a reduction in the population of the Fe³⁺ ground state (Fig. S3) as electrons are excited into Fe d orbitals in the GdFeO₃ conduction bands.¹⁰ Unlike in the 400 nm spectra, the negative absorption feature pumped with 800 nm excitation has a spectral blueshift at the Fe M_{2,3} edge from ~52.8 – 55.8 eV (blue) that begins shortly after photoexcitation. Following this spectral shift, a peak splitting results in a positive absorption feature (red, ~53.5 – 54.3 eV) within the Fe M_{2,3} edge in the 800 nm pumped spectra. Additionally, following 800 nm photoexcitation, there are several features that correspond to an increase in absorption (Fig. 2A) that appear from 50.3 – 52.8 eV and 56.3 – 58.0 eV. Transient increases in absorption are also present in the 400 nm pumped spectra (Fig. 2B) from ~52.6 – 52.9 and ~55.6 – 58.0 eV, though the lower energy positive absorption feature is narrower following 400 nm photoexcitation when compared to the 800 nm spectrum.

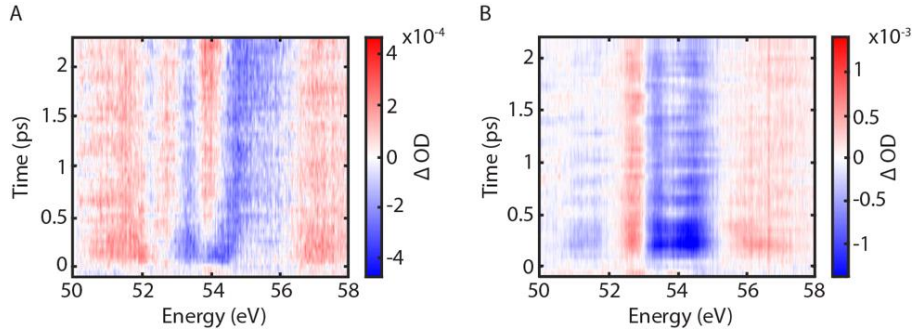


Figure 2. Transient XUV spectra following 800 nm (A) and 400 nm (B) photoexcitation. A decrease in absorption (blue feature) centered around 54 eV appears immediately following photoexcitation in both spectra and corresponds to the Fe $M_{2,3}$ edge.

Due to the strong contribution of angular momentum to the core-level transition Hamiltonian at the Fe $M_{2,3}$ edge, increases (red) and decreases (blue) in absorption in the XUV spectrum do not directly relate to electron and hole energies following photoexcitation, but instead relate to changes in oxidation state, phonon modes, and other structural distortions such as small polarons.^{10,12} To understand the origin of the spectral features at the Fe $M_{2,3}$ edge of $GdFeO_3$, we use a density functional theory and Bethe-Salpeter equation (DFT+BSE) approach to model the excited state X-ray edge dynamics. The method uses the Quantum ESPRESSO^{29,30} and the OCEAN^{31–33} (Obtaining Core Excitations from the Ab initio electronic structure and the NIST BSE solver) codes. We model charge transfer and semi-empirical polaronic states using this DFT+BSE approach. Additionally, we employ a defect supercell approach with hybrid and polaron self-interaction corrected exchange-correlation functionals (HSE06 and pSIC) to calculate ab initio polaronic distortions in $GdFeO_3$ which are also applied to our DFT+BSE framework (pSIC+DFT+BSE). The theoretical methods applied here are discussed in more detail in the Methods section and Supporting Information.

The charge localization of both electron and hole polarons from the defect supercell calculations (Fig. 1A) predicts that the electron polaron localizes on one single iron site. The hole polaron is less localized than the electron polaron, however, its charge density is predicted to be centered over an iron site. This suggests that LMCT polaron formation which has previously been measured in a range of iron oxide photocatalysts, is not the dominant mechanism of polaron formation in $GdFeO_3$. If LMCT polaron formation were present would follow a charge transfer between oxygen and iron, resulting in a hole polaron centered on oxygen and an electron polaron localized on iron. On the other hand, a MMCT polaron would induce both electron and hole polaron formation on iron centers. The defect supercell calculations indicate that MMCT polaron formation is the dominant mechanism in $GdFeO_3$, contrary to previously measured LMCT polarons in this class of photocatalysts.^{9,10,12}

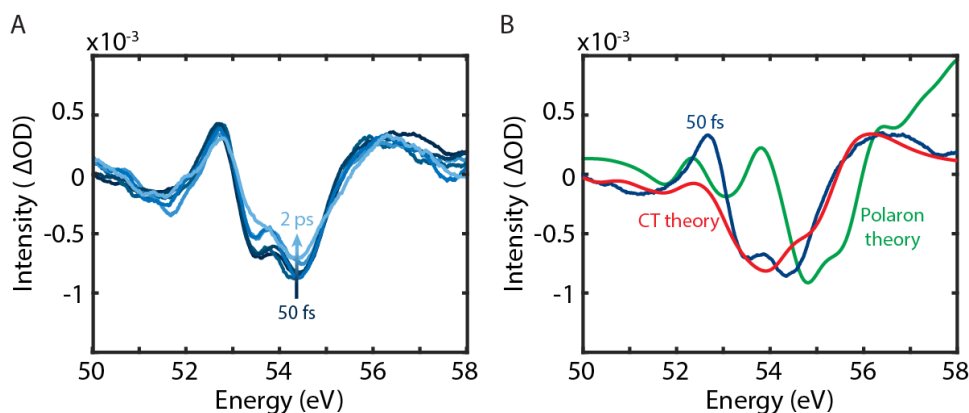


Figure 3. (A) Experimental lineouts from 50 fs (dark blue) to 2 ps (light blue) following 400 nm photoexcitation, sampled logarithmically. (B) Experimental lineout from 50 fs after 400 nm photoexcitation (blue) compared to DFT+BSE theory lineouts that model the 400 nm charge-transfer state (red) and an electron polaron state (green) show agreement with a charge-transfer state in the 400 nm spectra.

Figure 3 compares experimental lineouts at different time delays following 400 nm photoexcitation with DFT+BSE theory modeled 400 nm charge transfer and electron polaron states. There is good agreement between experimental lineouts at varying time delays following the 400 nm pump and the modeled 400 nm charge transfer state. There is very poor agreement between the 400 nm experimental lineouts and the DFT+BSE modeled polaron state that shifts to higher energy. The increases in absorption following 400 nm photoexcitation (Fig. 2B) from $\sim 52.6 - 52.9$ and $\sim 55.6 - 58.0$ eV are described by high-spin Fe^{2+} states forming as ligand to metal charge transfer (LMCT) from the oxygen to iron atoms occurs. Figure S9 in the supporting information presents ligand-field multiplet theory that agrees with this spin and oxidation state assignment.³⁴ The photoexcited LMCT state occurs on the same timescale as the pulse width and is present up to our temporal detection limit of 2 ns (Fig. S4). Our DFT+BSE and ligand-field multiplet theory, therefore, supports that LMCT following 400 nm photoexcitation forms a high-spin Fe^{2+} excited state, but strong coupling to phonons that would induce a polaronic lattice distortion is not present. The lack of a spectral shift to higher energies following 400 nm photoexcitation suggests that polaron formation is suppressed or so weak that it does not influence the transient spectra, and does not compete with the free carriers created during the charge transfer step (Fig. 3B, green line).^{10,12}

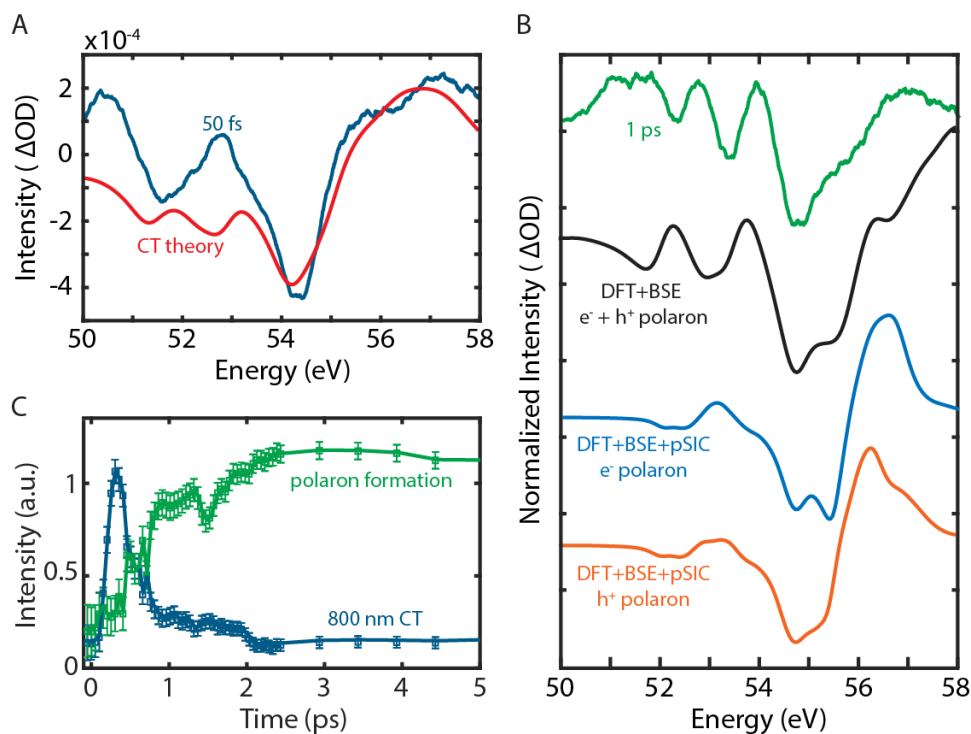


Figure 4. (A) Experimental lineout (blue) 50 fs after 800 nm photoexcitation and DFT+BSE theory calculated 800 nm charge-transfer state (red). (B) The polaron state that forms within a few hundred femtoseconds of 800 nm photoexcitation is modeled using DFT+BSE theory (black) for an electron and hole polaron and using the defect supercell pSIC+DFT+BSE theory for electron (blue) and hole (orange) polarons and is shown experimentally (green, 1 ps after 800 nm photoexcitation). Singular value decomposition (C) of the 800 nm pumped transient spectra reveals the kinetics of photoexcited polaron formation in GdFeO_3 .

The spectral lineout 50 fs after 800 nm photoexcitation in Figure 4A (blue) agrees well with DFT+BSE theory (red) for a modeled 800 nm charge transfer state. The DFT calculated PDOS (Fig. 1B) demonstrates that this excitation would originate from mixed O 2p/Fe 3d valence bands, and therefore could be either LMCT or MMCT in character. We find that the positive absorption features (Fig. 2A) at lower energies (50.0 – 52.8 eV) and higher energies (56.3 – 58.0 eV) in the 800 nm pumped spectra are associated with the creation of low-spin Fe^{2+} and high-spin Fe^{4+} states, respectively (Fig. S9). The formation of high-spin Fe^{4+} states in addition to low-spin Fe^{2+} states suggests that MMCT transitions are occurring between iron atoms following photoexcitation.²⁶ Section S9 in the supporting information discusses ligand-field multiplet theory that agrees with the assigned iron oxidation states and spin configurations in the transient XUV spectra.

Immediately following 800 nm photoexcitation, the Fe $M_{2,3}$ edge begins to shift towards higher energy. This spectral shift is most prominent from $\sim 54.4 - 56.0$ eV, is complete after $\sim 373 \pm 137$ fs (Fig. 4B), and has a magnitude of $\sim 423 \pm 122$ meV. Figure 4B shows agreement between experiment after the blueshift (green), DFT+BSE theory for a convolved electron and hole polaron (black), and pSIC+DFT+BSE theory for both electron (blue) and hole (orange) polarons at neighboring iron sites. The pSIC+DFT+BSE calculated electron and hole polarons occur at similar energies, suggesting that the electron and hole polarons are convolved spectrally. Singular value decomposition (SVD) in Figure 4C illustrates the transition of the charge transfer state to the

polaron state in the spectra and Figure S5 in the Supporting Information provides fitting of the spectral blueshift at the Fe $M_{2,3}$ edge. The SVD plot demonstrates that the charge transfer state transitions to the polaron state within the first picosecond following 800 nm photoexcitation.

In addition to the formation of photoexcited electron and hole polarons following 800 nm photoexcitation, a strong spectral splitting of the Fe $M_{2,3}$ edge feature occurs following polaron formation. The spectral splitting in the 800 nm spectra (Fig. 2A) results in an increase in absorption at $\sim 53.5 - 54.3$ eV that arises $\sim 330 \pm 52$ fs following photoexcitation. In the transient XUV spectra following 400 nm photoexcitation (Fig. 2B), there is spectral splitting that occurs at the Fe $M_{2,3}$ edge (53.8 eV), but it is weaker in intensity than the 800 nm photoexcitation, does not result in a positive signal, and does not change in intensity over time.

The spectral splitting can be attributed to t_{2g} and e_g crystal field splitting expected from the $GdFeO_3$ Fe^{3+} high-spin ground state (Fig. S3).^{25,35} This high-spin electronic configuration is preserved following 400 nm photoexcitation (Fig. S9), as demonstrated by the lack of change in spectral splitting between the ground state spectra and excited state 400 nm pumped spectra (Fig. 3A and Fig. S3). Additionally, the increases in absorption following 400 nm photoexcitation (Fig. 2B) result in the formation of an Fe^{2+} high-spin state, that appears as increases in absorption at $\sim 52.6 - 52.9$ and $\sim 55.6 - 58$ eV (Fig. S9). This indicates that the suppression of polaron formation following 400 nm photoexcitation is from the preservation of the spin state of the iron atoms following charge transfer.

In the case of 800 nm photoexcitation, the strong electron-phonon coupling induced by photoexcited electron and hole polarons influences the dynamics of spectral splitting at the Fe $M_{2,3}$ edge. This is evidenced by the t_{2g} and e_g crystal field splitting in the 800 nm pumped spectra (Fig. 2A) experiencing a transient increase in absorption at $\sim 53.5 - 54.3$ eV.³⁶ As demonstrated in the DFT+BSE and pSIC+DFT+BSE modeled spectra (Fig. 4B), the Fe^{2+} and Fe^{4+} centers created following MMCT begin forming electron and hole polarons, respectively. The hole polaron charge density is distributed across the oxygen and Fe^{4+} iron atom, while the electron polaron charge density is localized on the Fe^{2+} site (Fig. 1A). The distortion induced by the polarons is anisotropic (Fig. S8) and results in a Jahn-Teller distortion of the axial Fe-O ligands between the Fe-O-Fe bond length that is participating in polaron formation (Fig. 5A). The Jahn-Teller effect has been demonstrated to induce changes to Fe-O-Fe bond angles that are favorable for a superexchange interaction.³⁷⁻⁴⁰ We hypothesize that when the MMCT polaron forms after 800 nm excitation it induces a spin crossover from a high-spin electronic configuration to a low-spin electronic configuration on the Fe^{2+} centers, enabled by the Jahn-Teller effect and superexchange interaction.⁴¹⁻⁴³ This oxygen-ligand-mediated superexchange enables spins that would have otherwise been misaligned in a high-spin state on the neighboring iron atoms to be transferred as a spin crossover to a low-spin Fe^{2+} orbital configuration occurs.⁴⁴ This is supported by ligand-field multiplet theory modeling of both high-spin and low-spin configurations of Fe^{2+} and Fe^{4+} (Fig. S8), that agrees well with a low-spin Fe^{2+} configuration following photoexcitation. The Fe^{4+} feature at higher energies does not experience this spectral splitting, which suggests that the iron

that forms the hole polaron does not experience this spin crossover and remains in a high-spin configuration. This agrees with reports of delocalization, or “sharing”, of holes across a metal and ligand participating in superexchange.^{45,46} The octahedral site distortion in rare-earth orthoferrites is responsible for orbital and spin ordering, the modulation of that distortion through polaron formation enables this Fe-O-Fe superexchange following 800 nm photoexcitation.^{43,47,48} Figure 5B depicts the Fe t_{2g} and e_g orbital splitting changing as this spin crossover occurs, which is also observed spectrally (Fig. 2A).

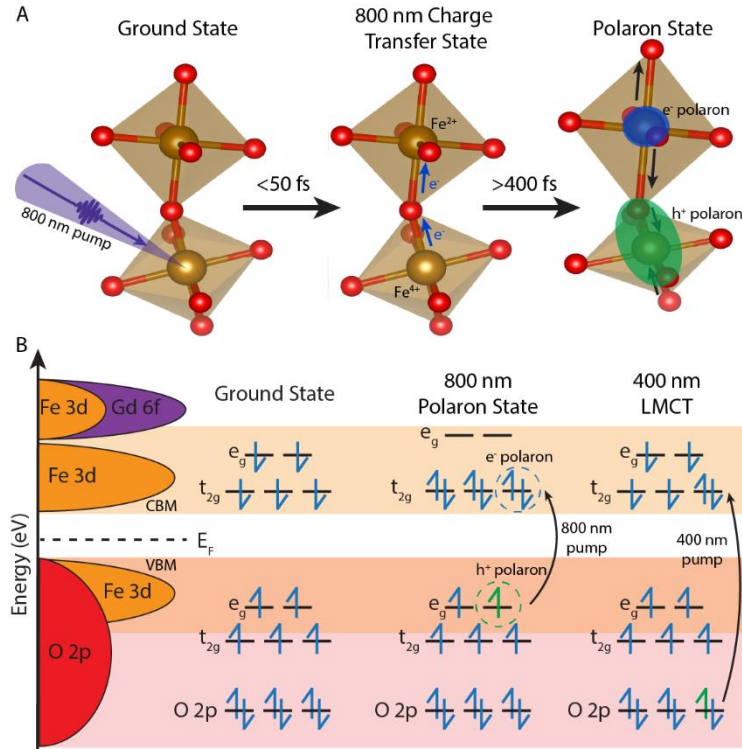


Figure 5. (A) Schematic of superexchange across the Fe-O-Fe bond that gives rise to spin crossover on Fe^{2+} centers during photoexcited polaron formation. Within the first 50 fs, the 800 nm charge transfer state results in a MMCT from one iron center to another across the Fe-O-Fe bond. After >400 fs, electron and hole polaron formation results in an expansion and contraction along the Fe-O-Fe bond length, that modulates its bond angle, inducing Jahn-Teller distortions and superexchange. (B) Diagram of t_{2g} and e_g splitting in the high-spin Fe^{3+} ground state (left), the low-spin Fe^{2+} and high-spin Fe^{4+} 800 nm excited state following photoexcited polaron formation (middle), and the high-spin Fe^{2+} excited state following 400 nm induced LMCT from O 2p orbitals (right).

As polaron formation does not occur during 400 nm photoexcitation, no Jahn-Teller distortion is induced on the iron octahedra, resulting in suppression of the superexchange interaction across the Fe-O-Fe bond. In the case of 400 nm photoexcitation, carriers are being excited predominantly from oxygen dominated valence bands causing a LMCT. The iron atoms remain in a high-spin configuration following LMCT, and polaron formation is suppressed, whereas an 800 nm photoexcitation induces polaron formation and a MMCT superexchange between neighboring iron atoms. This can be understood by Anderson’s exchange integral (J) in Equation (1):

$$J = 2n^{-2} \left[\frac{10}{3} Dq \right] U^{-1} \quad (1)^{49}$$

Where n is the spin state of the metal atom, Dq is the covalency of the orbital overlap integral, and U is the repulsive Coulomb interaction between single electrons. In the case of an 800 nm photoexcitation in GdFeO_3 , we excite from Fe dominated valence bands into Fe dominated conduction bands. The overlap and site-to-site hopping (Dq) between these orbitals is much greater than their on-site Coulomb repulsion (U).^{42,50,51} This enables the strong electron-phonon coupling, and subsequent deformation of the FeO_6 octahedra necessary for polaron formation and superexchange-based stabilization. Following a 400 nm pump, carriers are excited in GdFeO_3 from oxygen dominated valence bands into Fe d and Gd f dominated conduction bands. Here, $Dq \ll U$, as Fe and Gd both have strong on-site Coulombic repulsions.⁵² The U term dominates this exchange integral and suppresses superexchange and strong electron-phonon coupling. The results of this work present the exchange interaction as an additional parameter previously undiscussed to tune strong electron-phonon coupling effects in polar lattices.

Conclusion

Excitation-wavelength-dependent small polaron formation is measured in the intermediate insulator GdFeO_3 using transient XUV reflection spectroscopy. Photoexcitation with an 800 nm pump results in both electron and hole polaron formation at neighboring iron sites and strong spectral splitting at the Fe $M_{2,3}$ edge, indicative of a superexchange mediated spin crossover occurring on the iron atoms. A higher-energy 400 nm pump results in suppression of both superexchange and polaron formation due to strong on-site repulsions of the Fe and Gd atoms. This suggests a metal-metal polaron formation mechanism in which nearest neighbor iron sites form a hole and electron polaron through a superexchange across the Fe-O-Fe bond length. The ability to modulate polaron formation by varying excitation wavelength has been studied previously in hematite,¹⁰ however, this results in mostly changes to the mobility, lifetime, and recombination properties of the polaron as carriers populate different energy levels of the conduction bands. In the case of GdFeO_3 , we have suppressed photoexcited polaron formation with strong on-site repulsions following a higher-energy 400 nm photoexcitation, while inducing polaron formation when electron-phonon coupling is dominated by superexchange following 800 nm photoexcitation. We induce a superexchange-mediated spin crossover due to the Jahn-Teller distortion of the polaron following 800 nm photoexcitation. This spin-dependent modulation of polaron formation is of interest for applications that employ polarons for charge separation and for applications that would benefit from carrier mobility offered by suppression of polaron formation. Tuning spin properties and the exchange integral of these materials present an additional variable for controlling polaron formation in this class of highly polar materials. From a materials engineering perspective, polaronic tunability merits further study in intermediate and Mott-Hubbard insulating transition metal oxide materials.

Methods

Synthesis of single-crystalline GdFeO_3

Single crystals of GdFeO₃ were synthesized using the flux method, employing PbO, PbF₂, PbO₂, and B₂O₃ as fluxes in a high-temperature furnace. A stoichiometric mixture of Gd₂O₃ and Fe₂O₃ powders was thoroughly combined with the flux compounds and placed in a platinum crucible. The mixture was heated to 1250 °C for 16 h to ensure complete dissolution. Then, it was cooled slowly to 850 °C at a rate of 2 °C/h, and further cooled to room temperature at a rate of 100 °C/h. This process yielded large cuboid shaped GdFeO₃ crystals, with individual crystals obtaining lengths of up to 1 cm on a side.

Transient extreme ultraviolet (XUV) spectroscopy

For both photoexcitation wavelengths, the pump pulses are ~50-fs with a fluence of ~11 mJ/cm² and are time-delayed with respect to the probe pulse. The XUV probe pulse is generated by high harmonic generation in Ar gas from a few-cycle white light pulse. The transient extreme ultraviolet reflection experiment employs a 10° grazing incidence geometry, which results in a ~2 nm penetration depth.⁵³ The Fe M_{2,3} edge at ~54 eV corresponds to transitions from the 3p_{3/2,5/2} core levels into 3d core levels. The change in transient reflection following photoexcitation is defined by $\Delta OD = -\log_{10}(I_{\text{pump on}}/I_{\text{pump off}})$. Additional details about the transient extreme ultraviolet spectrometer can be found in the Supporting Information.

Ab initio polaron and core-level spectra modeling

The theoretical framework we employ to fully analyze the transient core-level spectra has been described in detail previously.²¹ We compute both the ground state X-ray absorption at the Fe M_{2,3} edge in GdFeO₃ and differential effects to the core-level GdFeO₃ spectra following excitation-wavelength-dependent photoexcitation and polaron formation. These effects are calculated with an ab initio theoretical approach which employs density functional theory and the Bethe-Salpeter equation (DFT+BSE). The DFT+BSE approach employs DFT using the Quantum ESPRESSO package^{29,30} and the existing OCEAN code^{31–33} (Obtaining Core-level Excitations using Ab-initio calculations and the NIST BSE solver) for the BSE, which we have modified to use excited state distributions to determine transient changes in the XUV spectra. We first calculate the band structure of GdFeO₃ using DFT. Then, the BSE is solved to obtain the core-valence exciton wavefunctions and transient XUV spectra can be plotted from the complex dielectric function calculated by OCEAN. A modification to the OCEAN code, discussed previously,^{21,54} enables the calculation of excited state dynamics and is employed to model the initial charge transfer states. Polaronic distortions are modeled using a DFT+BSE approach where we apply a semi-empirical distortion to an FeO₆ octahedra and calculate its resulting Fe M_{2,3} edge spectra, polaronic distortions calculated using this technique are termed DFT+BSE. We further model polaronic lattice distortions using a defect supercell approach with hybrid and polaron self-interaction corrected exchange-correlation functionals (HSE06 and pSIC) as implemented in the VASP code.^{55–59} These functionals either incorporate a fraction of Hartree-Fock (HF) exact exchange to improve self-interaction errors and a description of charge localization (e.g. hybrid functionals) that depends on an empirical parameter (α , the HF mixing parameter), or employ a variational approach from a closed-shell system for a parameter-free ab initio methodology for calculating

polaron properties that removes the sensitivity to empirical parameters like α or Hubbard U parameters.⁵⁶ These methods were used to identify structural distortions and relative energetics associated with electron and hole polaron formation at different sites in GdFeO₃ and to assess their sensitivity to empirical parameters in the calculations. We generally refer to the polaron-containing structures and subsequent X-ray spectra obtained via these approaches (hybrid functionals and/or with the pSIC approach) as pSIC+DFT+BSE. Additional details about ab initio modeling of photoexcited XUV dynamics can be found in the Supporting Information section.

Author Information

Corresponding Author

Scott K. Cushing – Division of Chemistry and Chemical Engineering, California Institute of Technology, Pasadena, California 91125, United States

Authors

Jocelyn L. Mendes – Division of Chemistry and Chemical Engineering, California Institute of Technology, Pasadena, California 91125, United States

Hyun Jun Shin – Department of Physics, Yonsei University, Seoul, 03722, Republic of Korea

Jae Yeon Seo – Department of Physics, Yonsei University, Seoul, 03722, Republic of Korea

Nara Lee – Department of Physics, Yonsei University, Seoul, 03722, Republic of Korea

Young Jai Choi – Department of Physics, Yonsei University, Seoul, 03722, Republic of Korea

Joel B. Varley – Lawrence Livermore National Laboratory, Livermore, California 94550, United States

Acknowledgements

This material is based on work performed by the Liquid Sunlight Alliance, which is supported by the U.S. Department of Energy, Office of Science, Office of Basic Energy Sciences, Fuels from Sunlight Hub under Award Number DE-SC0021266. This research used resources of the National Energy Research Scientific Computing Center a DOE Office of Science User Facility supported by the Office of Science of the U.S. Department of Energy under Contract No. DE-AC02-05CH11231 using NERSC award BES-ERCAP0024109. The computations presented here were, in part, conducted in the Resnick High Performance Computing Center, a facility supported by Resnick Sustainability Institute at the California Institute of Technology. The ground state optical absorption of GdFeO₃ was collected at the Molecular Materials Research Center in the Beckman Institute of the California Institute of Technology. J.L.M. acknowledges support by the National Science Foundation Graduate Research Fellowship Program under grant no. 1745301. GdFeO₃ synthesis and characterization carried out at Yonsei University was supported by the National

Research Foundation of Korea (NRF) through grants NRF-2021R1A2C1006375, and NRF-2022R1A2C1006740. The work of J.B.V. was performed under the auspices of the US DOE by Lawrence Livermore National Laboratory under contract DE-AC52-07NA27344 and supported by the HydroGEN Advanced Water Splitting Materials Consortium, established as part of the Energy Materials Network under the U.S. Department of Energy (DOE), the Office of Energy Efficiency and Renewable Energy (EERE), the Hydrogen and Fuel Cell Technologies Office (HFTO).

Notes

The authors declare no competing financial interests.

References

1. Franchini, C., Reticcioli, M., Setvin, M. & Diebold, U. Polarons in materials. *Nat. Rev. Mater.* **6**, 560–586 (2021).
2. Cheng, C., Zhou, Z. & Long, R. Time-domain view of polaron dynamics in metal oxide photocatalysts. *J. Phys. Chem. Lett.* **14**, 10988–10998 (2023).
3. Suntivich, J. *et al.* Probing intermediate configurations of oxygen evolution catalysis across the light spectrum. *Nat. Energy* 1–8 (2024) doi:10.1038/s41560-024-01583-x.
4. Rettie, A. J. E., Chemelewski, W. D., Emin, D. & Mullins, C. B. Unravelling small-polaron transport in metal oxide photoelectrodes. *J. Phys. Chem. Lett.* **7**, 471–479 (2016).
5. Pastor, E. *et al.* Electronic defects in metal oxide photocatalysts. *Nat. Rev. Mater.* **7**, 503–521 (2022).
6. Emin, D. *Polarons* (Cambridge University Press, 2012).
7. Yazdani, N. *et al.* Coupling to octahedral tilts in halide perovskite nanocrystals induces phonon-mediated attractive interactions between excitons. *Nat. Phys.* **20**, 47–53 (2024).
8. Ghosh, R. & Spano, F. C. Excitons and polarons in organic materials. *Acc. Chem. Res.* **53**, 2201–2211 (2020).
9. Biswas, S., Wallentine, S., Bandaranayake, S. & Baker, L. R. Controlling polaron formation at hematite surfaces by molecular functionalization probed by XUV reflection-absorption spectroscopy. *J. Chem. Phys.* **151**, 104701 (2019).
10. Carneiro, L. M. *et al.* Excitation-wavelength-dependent small polaron trapping of photoexcited carriers in α -Fe₂O₃. *Nat. Mater.* **16**, 819–825 (2017).
11. Vura-Weis, J. *et al.* Femtosecond M_{2,3}-edge spectroscopy of transition-metal oxides: photoinduced oxidation state change in α -Fe₂O₃. *J. Phys. Chem. Lett.* **4**, 3667–3671 (2013).
12. Kim, Y.-J. *et al.* Coherent charge hopping suppresses photoexcited small polarons in ErFeO₃ by antiadiabatic formation mechanism. *Sci. Adv.* **10**, eadk4282 (2024).
13. Bandaranayake, S., Hruska, E., Londo, S., Biswas, S. & Baker, L. R. Small polarons and surface defects in metal oxide photocatalysts studied using XUV reflection-absorption spectroscopy. *J. Phys. Chem. C* **124**, 22853–22870 (2020).
14. Husek, J., Cirri, A., Biswas, S. & Baker, L. R. Surface electron dynamics in hematite (α -Fe₂O₃): correlation between ultrafast surface electron trapping and small polaron formation. *Chem. Sci.* **8**, 8170–8178 (2017).

15. Gajapathy, H. *et al.* Spin polarized electron dynamics enhance water splitting efficiency by yttrium iron garnet photoanodes: a new platform for spin selective photocatalysis. *Chem. Sci.* **15**, 3300–3310 (2024).
16. Bu, X. & Li, Y. Optical signature for distinguishing between Mott-Hubbard, intermediate, and charge-transfer insulators. *Phys. Rev. B* **106**, L241101 (2022).
17. Zhu, X.-H., Xiao, X.-B., Chen, X.-R. & Liu, B.-G. Electronic structure, magnetism and optical properties of orthorhombic GdFeO₃ from first principles. *RSC Adv.* **7**, 4054–4061 (2017).
18. Khan, H. & Ahmad, T. Perspectives and scope of ABO₃ type multiferroic rare-earth perovskites. *Chin. J. Phys.* **91**, 199–219 (2024).
19. Podlesnyak, A., Nikitin, S. E. & Ehlers, G. Low-energy spin dynamics in rare-earth perovskite oxides. *J. Phys. Condens. Matter* **33**, 403001 (2021).
20. Li, H. *et al.* Degree of geometric tilting determines the activity of FeO₆ octahedra for water oxidation. *Chem. Mater.* **30**, 4313–4320 (2018).
21. Klein, I. M., Liu, H., Nimlos, D., Krotz, A. & Cushing, S. K. Ab initio prediction of excited-state and polaron effects in transient XUV measurements of α -Fe₂O₃. *J. Am. Chem. Soc.* **144**, 12834–12841 (2022).
22. Cashion, J. D., Cooke, A. H., Martin, D. M. & Wells, M. R. Magnetic interactions in gadolinium orthoferrite. *J. Phys. C: Solid State Phys.* **3**, 1612 (1970).
23. Das, M., Roy, S. & Mandal, P. Giant reversible magnetocaloric effect in a multiferroic GdFeO₃ single crystal. *Phys. Rev. B* **96**, 174405 (2017).
24. Paul, P., Ghosh, P. S., Rajarajan, A. K., Babu, P. D. & Rao, T. V. C. Ground state spin structure of GdFeO₃: A computational and experimental study. *J. Magn. Magn. Mater.* **518**, 167407 (2021).
25. Yuan, X., Sun, Y. & Xu, M. Effect of Gd substitution on the structure and magnetic properties of YFeO₃ ceramics. *J. Solid State Chem.* **196**, 362–366 (2012).
26. Mikhaylovskiy, R. V. *et al.* Resonant pumping of d–d crystal field electronic transitions as a mechanism of ultrafast optical control of the exchange interactions in iron oxides. *Phys. Rev. Lett.* **125**, 157201 (2020).
27. Panuganti, S. *et al.* Transient X-ray diffraction reveals nonequilibrium phase transition in thin films of CH₃NH₃PbI₃ perovskite. *ACS Energy Lett.* **8**, 691–698 (2023).
28. Zhang, J., Shi, J., Chen, Y., Zhang, K. H. L. & Yang, Y. Bimolecular self-trapped exciton formation in bismuth vanadate. *J. Phys. Chem. Lett.* **13**, 9815–9821 (2022).
29. Giannozzi, P. *et al.* QUANTUM ESPRESSO: a modular and open-source software project for quantum simulations of materials. *J. Phys. Condens. Matter* **21**, 395502 (2009).
30. Giannozzi, P. *et al.* Advanced capabilities for materials modelling with Quantum ESPRESSO. *J. Phys. Condens. Matter* **29**, 465901 (2017).
31. Vinson, J. Advances in the OCEAN-3 spectroscopy package. *Phys. Chem. Chem. Phys.* **24**, 12787–12803 (2022).
32. Vinson, J., Rehr, J. J., Kas, J. J. & Shirley, E. L. Bethe-Salpeter equation calculations of core excitation spectra. *Phys. Rev. B* **83**, 115106 (2011).
33. Gilmore, K. *et al.* Efficient implementation of core-excitation Bethe–Salpeter equation calculations. *Comput. Phys. Commun.* **197**, 109–117 (2015).
34. Stavitski, E. & de Groot, F. M. F. The CTM4XAS program for EELS and XAS spectral shape analysis of transition metal L edges. *Micron* **41**, 687–694 (2010).

35. Khalil, M. *et al.* Picosecond X-ray absorption spectroscopy of a photoinduced iron(II) spin crossover reaction in solution. *J. Phys. Chem. A* **110**, 38–44 (2006).
36. Zhang, K., Ash, R., Girolami, G. S. & Vura-Weis, J. Tracking the metal-centered triplet in photoinduced spin crossover of Fe(phen)₃²⁺ with tabletop femtosecond M-edge X-ray absorption near-edge structure spectroscopy. *J. Am. Chem. Soc.* **141**, 17180–17188 (2019).
37. Takada, Y. & Masaki, M. Polarons in Jahn–Teller crystals: intrinsic difference between e_g and t_{2g} electrons. *J. Supercond. Nov. Magn.* **20**, 629–633 (2007).
38. Sudandararaj, A. T. S., Kumar, G. S., Dhivya, M., Eithiraj, R. D. & Banu, I. B. S. Band structure calculation and rietveld refinement of nanoscale GdFeO₃ with affirmation of Jahn Teller’s distortion on electric and magnetic properties. *J. Alloys Compd.* **783**, 393–398 (2019).
39. Panchwanee, A., Reddy, V. R., Gupta, A., Bharathi, A. & Phase, D. M. Study of local distortion and spin reorientation in polycrystalline Mn doped GdFeO₃. *J. Alloys Compd.* **745**, 810–816 (2018).
40. Kim, B. H. & Min, B. I. Nearest and next-nearest superexchange interactions in orthorhombic perovskite manganites RMnO₃ (R= rare earth). *Phys. Rev. B* **80**, 064416 (2009).
41. Feinberg, D., Germain, P., Grilli, M. & Seibold, G. Joint superexchange–Jahn-Teller mechanism for layered antiferromagnetism in LaMnO₃. *Phys. Rev. B* **57**, R5583–R5586 (1998).
42. Anderson, P. W. Antiferromagnetism. Theory of superexchange interaction. *Phys. Rev.* **79**, 350–356 (1950).
43. Zhou, J.-S. *et al.* Intrinsic structural distortion and superexchange interaction in the orthorhombic rare-earth perovskites RCrO₃. *Phys. Rev. B* **81**, 214115 (2010).
44. Mikhaylovskiy, R. V. *et al.* Ultrafast optical modification of exchange interactions in iron oxides. *Nat. Commun.* **6**, 8190 (2015).
45. Occhialini, C. A. *et al.* Nature of excitons and their ligand-mediated delocalization in nickel dihalide charge-transfer insulators. *Phys. Rev. X* **14**, 031007 (2024).
46. Takubo, K. *et al.* Unusual superexchange pathways in an NiS₂ triangular lattice with negative charge-transfer energy. *Phys. Rev. Lett.* **99**, 037203 (2007).
47. Zhou, J.-S. & Goodenough, J. B. Intrinsic structural distortion in orthorhombic perovskite oxides. *Phys. Rev. B* **77**, 132104 (2008).
48. Eibschütz, M., Shtrikman, S. & Treves, D. Mössbauer studies of Fe⁵⁷ in orthoferrites. *Phys. Rev.* **156**, 562–577 (1967).
49. Anderson, P. W. New approach to the theory of superexchange interactions. *Phys. Rev.* **115**, 2–13 (1959).
50. Kanamori, J. Superexchange interaction and symmetry properties of electron orbitals. *J. Phys. Chem. Solids* **10**, 87–98 (1959).
51. Whangbo, M.-H., Koo, H.-J., Dai, D. & Jung, D. Effect of metal–ligand bond lengths on superexchange interactions in Jahn–Teller d⁴ ion systems: Spin dimer analysis of the magnetic structure of marokite CaMn₂O₄. *Inorg. Chem.* **41**, 5575–5581 (2002).
52. Bashir, A., Ikram, M., Kumar, R. & Lisboa-Filho, P. N. Structural, electronic structure and magnetic studies of GdFe_{1-x}Ni_xO₃ (x ≤ 0.5). *J. Alloys Compd.* **521**, 183–188 (2012).
53. Liu, H. *et al.* Measuring photoexcited electron and hole dynamics in ZnTe and modeling excited state core-valence effects in transient extreme ultraviolet reflection spectroscopy. *J. Phys. Chem. Lett.* **14**, 2106–2111 (2023).

54. Klein, I. M., Krotz, A., Lee, W., Michelsen, J. M. & Cushing, S. K. Ab initio calculations of XUV ground and excited states for first-row transition metal oxides. *J. Phys. Chem. C* **127**, 1077–1086 (2023).
55. Sadigh, B., Erhart, P. & Åberg, D. Variational polaron self-interaction-corrected total-energy functional for charge excitations in insulators. *Phys. Rev. B* **92**, 075202 (2015).
56. Heyd, J., Scuseria, G. E. & Ernzerhof, M. Hybrid functionals based on a screened Coulomb potential. *J. Chem. Phys.* **118**, 8207–8215 (2003).
57. Zhou, F., Sadigh, B., Erhart, P. & Åberg, D. Ab initio prediction of fast non-equilibrium transport of nascent polarons in SrI₂: a key to high-performance scintillation. *Npj Comput. Mater.* **2**, 1–7 (2016).
58. Paier, J., Marsman, M., Hummer, K., Kresse, G., Gerber, I. C., Angyan, J. G. Screened hybrid density functionals applied to solids. *J. Chem. Phys.* **124**, 154709 (2006).
59. Varley, J. B., Janotti, A., Franchini, C. & Van de Walle, C. G. Role of self-trapping in luminescence and *p*-type conductivity of wide-band-gap oxides. *Phys. Rev. B* **85**, 081109 (2012).

Supporting Information for:

**Dynamic Competition Between Orbital and Exchange Interactions
Selectively Localizes Electrons and Holes Through Polarons**

Jocelyn L. Mendes¹, Hyun Jun Shin², Jae Yeon Seo², Nara Lee², Young Jai Choi², Joel B. Varley³, and Scott K. Cushing^{1*}

¹ Division of Chemistry and Chemical Engineering, California Institute of Technology, Pasadena, California 91125, United States

² Department of Physics, Yonsei University, Seoul, 03722, Republic of Korea

³ Lawrence Livermore National Laboratory, Livermore, California 94550, United States

*Correspondence and requests for materials should be addressed to S.K.C. (email: scushing@caltech.edu)

Supporting Information Contents

S1. GdFeO₃ characterization.....	19
S1.1 Ground State Optical Characterization	19
S1.2 Structural Characterization	19
S2. Experimental Setup: Transient Extreme Ultraviolet Reflectivity Spectrometer	20
S3. Theoretical Methods: Ground State and Excited State Core-Level Spectra	23
S3.1. Density Functional Theory Calculations	23
S3.2. Defect supercell calculations.....	24
S3.3. Fe M_{2,3} Edge Ground State Calculation	25
S3.4. Fe M_{2,3} edge Excited and Thermal State Calculations.....	25
S3.5. Fe M_{2,3} Edge DFT+BSE Polaron State Calculations.....	26
S3.6. Fe M_{2,3} Edge pSIC+DFT+BSE Polaron State Calculations.....	27
S4. Ligand-Field Multiplet Theory Calculations.....	27
References	28

S1. GdFeO₃ characterization

S1.1 Ground State Optical Characterization

The band gap of single-crystal GdFeO₃ was determined using UV-Visible reflection spectroscopy (Cary 5000, Agilent Technologies). Scans were collected in a range of 250-1200 nm in reflectivity mode. For a Tauc plot analysis, the reflectance spectra were transformed using the Kubelka-Munk function using **Equation S1**:

$$F(R_{\infty}) = \frac{(1-R_{\infty})^2}{2R_{\infty}} \quad (\text{S1})$$

where $R_{\infty} = R_{\text{sample}}/R_{\text{standard}}$.¹ The direct band gap of GdFeO₃ was measured as ~1.425 eV and the indirect band gap was measured to be ~1.390 eV.

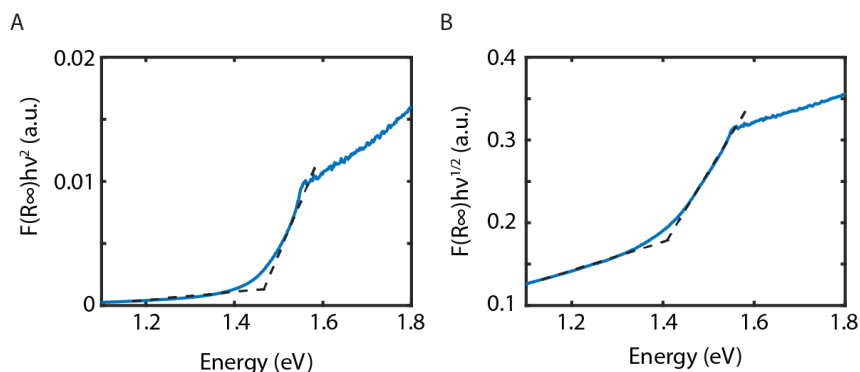


Figure S1. Tauc plot from the measured optical ground state reflectivity of GdFeO₃ with $(\alpha h\nu)^{1/r}$ plotted as $r = 1/2$ for a direct allowed band gap transition (A) and $r = 2$ for an indirect allowed band gap transition (B). The direct band gap is found to be ~1.425 eV and the indirect band gap is found to be ~1.390 eV.

S1.2 Structural Characterization

The crystallographic structure and absence of a second phase were checked by the Rietveld refinement using the FullProf program for the powder X-ray diffraction data. The data were obtained with a Rigaku D/Max 2500 powder X-ray diffractometer using Cu-K _{α} radiation. The result suggests that the GdFeO₃ forms an orthorhombic perovskite with the *Pbnm* space group. The lattice constants are found to be $a = 5.3464 \text{ \AA}$, $b = 5.5996 \text{ \AA}$, and $c = 7.6623 \text{ \AA}$ with the reliability factors; $\chi^2 = 1.64$, $R_p = 2.29 \%$, $R_{wp} = 3.03 \%$, and $R_{exp} = 2.37 \%$. Further details of crystallographic data are summarized in **Table S1**.

Table S1. Crystallographic information of GdFeO₃. Unit cell parameters, reliability factors and position parameters for GeFeO₃.

Structure	Orthorhombic
Space group	<i>Pbnm</i>
Lattice parameters (Å)	$a = 5.3464(1)$
	$b = 5.5996(1)$
	$c = 7.6623(2)$
	$c/a = 1.433$
R-factors (%)	$R_p = 2.29$
	$R_{wp} = 3.03$
	$R_{exp} = 2.37$
χ^2	1.64
Gd (x, y, z)	(1.0159, 0.0605, 0.25)
Fe (x, y, z)	(0.5, 0, 0)
O ₁ (x, y, z)	(0.4219, 0.9627, 0.25)
O ₂ (x, y, z)	(0.7107, 0.2988, 0.0455)

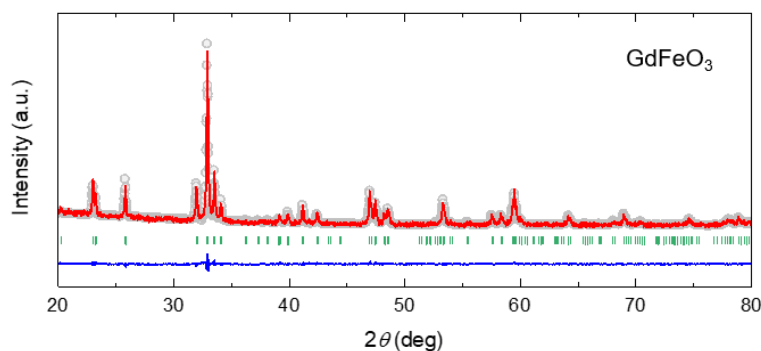


Figure S2. X-ray diffraction pattern of single-crystalline GdFeO₃. The observed (gray circles) and calculated (red solid line) powder X-ray diffraction patterns for a GdFeO₃ single crystal at 293 K. The blue curve denotes the difference in intensity between the observed and calculated patterns, while the short green ticks indicate the Bragg reflection positions.

S2. Experimental Setup: Transient Extreme Ultraviolet Reflectivity Spectrometer

The transient extreme ultraviolet (XUV) reflectivity spectrometer is described previously.^{2,3} Briefly, a Legend Elite Duo laser system (Coherent Inc.) with 35 fs, 13 mJ, 1 kHz pulses centered at 800 nm is split by a 75:25 beam splitter with ~3 mJ being used to generate a few-cycle white light beam (<6 fs, 550-900 nm) for high harmonic generation (HHG) and ~10 mJ used for the

pump path. The pump path uses both a p-polarized 800 nm beam and the 400 nm frequency doubled output of a BBO crystal with p-polarization, pumped with the 800 nm output of the Ti:Sapphire laser. The optical excitation fluence used in these experiments was $\sim 11 \text{ mJ/cm}^2$ for both 400 nm and 800 nm pumped samples. Transient reflection is measured at a 10° grazing incidence (80° from normal incidence) geometry and measures the varying delay times between the pump and probe pulses by an optomechanical delay stage. The photoexcited dynamics were probed with an XUV pulse produced with an s-polarized few-cycle white light pulse by HHG in argon. The residual white light beam is removed with a 200 nm thick Al filter (Luxel). The generated XUV continuum is used to probe the Fe $M_{2,3}$ absorption edges at $\sim 54 \text{ eV}$. An edge-pixel referencing scheme was used to denoise the spectra due to intensity fluctuations and used signal-free spectral regions.⁴

The ground state sample reflectivity at the Fe $M_{2,3}$ edge is shown in **Figure S3**. The experimental spectrum (**Figure S3**, orange line) was smoothed using a moving average filter with a span of 2.0% of the pixels in the CCD image. The static XUV reflectivity of GdFeO_3 is obtained by normalizing the static XUV reflectivity spectrum of the sample by the static reflectivity of a Si wafer, which should not absorb the XUV beam below the Si K edge at $\sim 100 \text{ nm}$. The spectrometer was calibrated using the photoionization continuum of neon gas.⁵

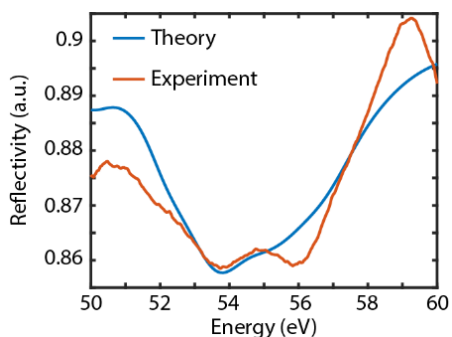


Figure S3. Experimental ground state XUV reflectivity spectrum (orange) and DFT+BSE theory calculated ground state reflectivity (blue).

The transient spectra presented in the main text (**Figure 2**) capture the relevant ultrafast features of charge transfer, polaron formation, and the superexchange induced spin crossover on Fe^{2+} centers. Additionally, we present here representative spectra of long timescale dynamics measured at the Fe $M_{2,3}$ X-ray edge following 800 and 400 nm photoexcitation to understand thermalization in the spectra. **Figure S4A** and **S4B** presents logarithmic spectra collected out to 1 ns. We compare

the long timescale 800 and 400 nm pumped spectra to our DFT+BSE treatment of thermal expansion of the GdFeO_3 crystal lattice (**Fig. S4C** and **S4D**) and to our modeled charge transfer and polaron states. The polaron state dominates the 800 nm pumped GdFeO_3 spectra out to 1 ns (**Fig. S4C**), which suggests that thermal expansion of the lattice plays a minimal role in the observed spectral features. Similarly, the DFT+BSE modeled 400 nm charge transfer state (**Fig. S4D**) continues to dominate the 400 nm pumped transient XUV spectrum, out to 1 ns. This suggests that the free carriers in the charge transfer state dominate the 400 nm pumped spectrum out to our temporal measurement limit.

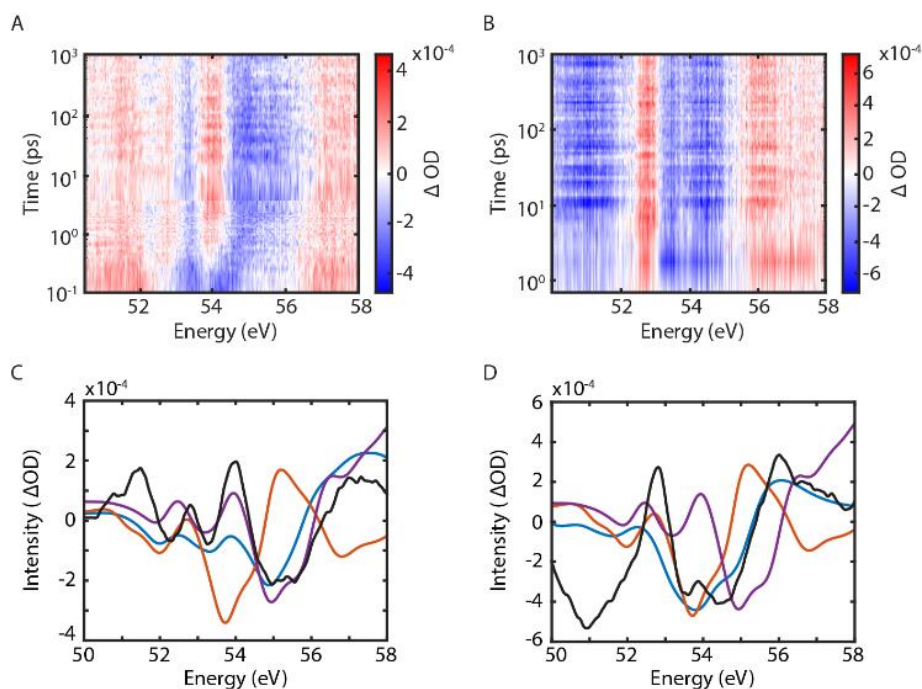


Figure S4. Long timescale measurements of GdFeO_3 following 800 nm (A) and 400 nm (B) photoexcitation are plotted on a logarithmic time axis. Experimental lineouts 1 ns after 800 nm (C, black) and 400 nm (D, black) photoexcitation are compared to DFT+BSE modeled 800 and 400 nm charge transfer states (blue), the convolved electron and hole polaron state (purple), and a modeled 350 K thermal expansion of the crystal lattice (red). For the 800 nm spectrum (C) the polaron state best agrees with the 1 ns experimental trace, while the 400 nm spectrum (D) agrees well with the 400 nm charge transfer state.

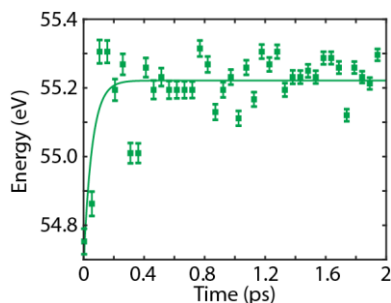


Figure S5. A fit of the spectral shift at the Fe $M_{2,3}$ edge following 800 nm photoexcitation. The fitting was performed by finding the minima of the spectral intensity between 54.0 – 55.0 eV and results in an exponential fit following the equation: $a \cdot \exp(-x./b)+c$, where $a = -0.5417$, $b = 0.0541$, and $c = 55.32$.

S3. Theoretical Methods: Ground State and Excited State Core-Level Spectra

S3.1. Density Functional Theory Calculations

Geometry optimization and density functional theory (DFT) were conducted using the Quantum ESPRESSO package with norm-conserving general gradient approximation (GGA), Perdew-Burke-Ernzerhof (PBE) pseudopotentials.^{6–8} Geometry optimizations employed an input $GdFeO_3$ unit cell containing 20 atoms and based upon the experimental crystallographic information listed in **Table S1**. A 250 Rydberg kinetic energy cutoff and an $11 \times 10 \times 7$ Monkhorst–Pack k-mesh sampling of the first Brillouin zone was used to sample 200 bands. The starting magnetization was set to a sum of zero for Fe^{3+} ions to represent the antiferromagnetic orientation of neighboring spins at 293 K.⁹ A Hubbard U parameter of 4 eV and 5 eV was applied to Fe and Gd atoms respectively for DFT and DFT+BSE calculations. The structures employed in the DFT and DFT+BSE calculations described below were fully relaxed and calculations were performed to a convergence of 10^{-8} eV/atom with the forces on ions under 10^{-3} eV/Å.

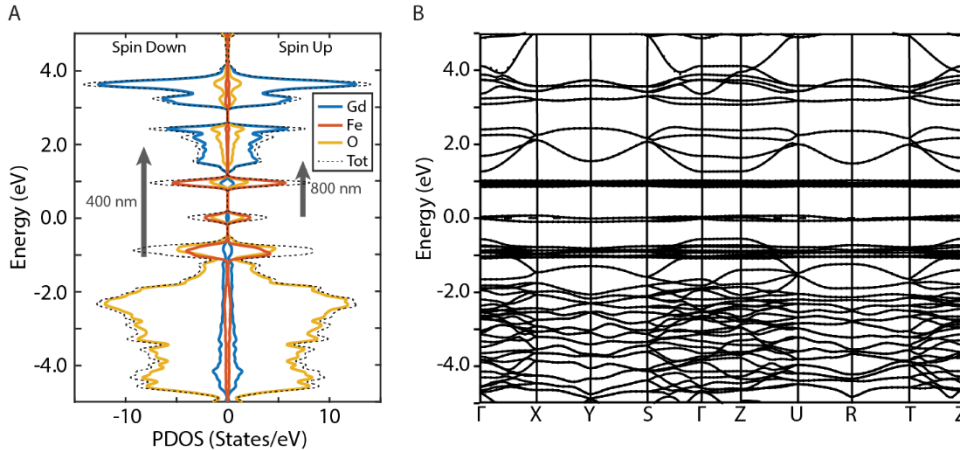


Figure S6. DFT+U calculated projected density of states (A), and band structure (B) used for DFT+BSE calculations of core-level spectra.

S3.2. Defect supercell calculations

Hole and electron polarons were modeled within a supercell approach,¹⁰ using a $2 \times 2 \times 1$ repetition of the optimized unit cells (160-atom supercells) calculated for an antiferromagnetic spin ordering ground state. The defect supercell calculations with pSIC and hybrid functionals were performed using the VASP code version 5.4,¹¹ using the HSE06 screened hybrid functional,^{12,13} the implemented pSIC approach,^{14,15} and the projector augmented wave (PAW) approach with the VASP4 PAW_PBE potentials (Fe_pv : 14 valence electrons, Gd: 18 valence electrons, and O: 6 valence electrons).^{16,17} All supercell simulations adopted a plane-wave energy cutoff of 400 eV, and evaluated energies with a single special k -point at 0.25, 0.25, 0.25. Simulations with DFT+U with pSIC adopted a Hubbard U value only for the Fe d states with a value of 5.3 as based on default parameters used for the Materials Project database.^{18,19} All structure initial structures were optimized from unit cells with an antiferromagnetic ground state with magnetic moments of 4.8 and 7.2 for the Fe and Gd, respectively, with final moments of approximately 4 and 7 obtained for the bulk for the studied levels of theory. The lattice constants for the supercells with self-consistently determined for each level of theory, with the impact of the fraction of exact change on the electronic band included in **Figure S7**.

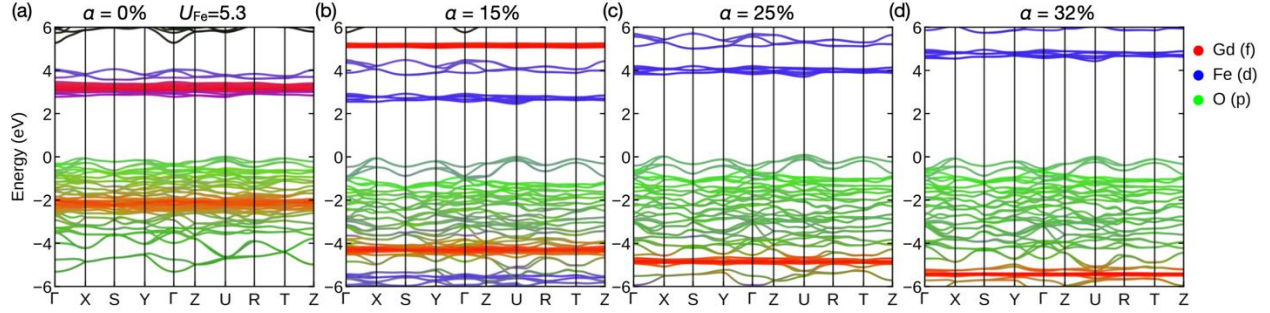


Figure S7. Summary of variations in the electronic structure for GdFeO₃, shown at different levels of theory from PBE+U (a) to HSE06 with different levels of exact exchange such as 15% (b), 25% (c) and 32% (d). The primary impact of exact exchange is widening of the band gap between the upper valence band (Fe and O derived) and the localized Fe-d derived band, with the separation between the latter band and a higher-lying conduction band (Fe and Gd derived) remaining largely ~ 1 eV higher, independent of the exact exchange.

S3.3. Fe M_{2,3} Edge Ground State Calculation

The fully relaxed parameters used in the DFT+U calculations for GdFeO₃ discussed in S4.1 were applied to the DFT+BSE calculations of the GdFeO₃ ground state reflectivity at the Fe M_{2,3} X-ray edge. The BSE calculation employed a screening mesh of $2 \times 2 \times 2$, a dielectric constant of 4.28 at 293 K,⁹ a 4.0 Bohr screening radius, and a 0.7 scaling factor for the Slater G parameter. A spectral broadening of 0.25 eV was applied for all calculated spectra. The calculated ground state reflectivity of GdFeO₃ is plotted in Figure S3 and is compared to the experimentally measured XUV ground state at the Fe M_{2,3} X-ray edge. As shown in Figure S3, the DFT+BSE calculated ground state agrees well with the measured ground state reflectivity of the GdFeO₃ sample.

S3.4. Fe M_{2,3} edge Excited and Thermal State Calculations

Excitation-wavelength-dependent changes to the transient XUV spectra of GdFeO₃ were calculated using a modification to the OCEAN package described previously.^{3,20–22} Effectively, the modification to the OCEAN code enables us to selectively allow or forbid core-to-valence X-ray transitions to valence and conduction bands at different points in momentum space, to simulate state-filling of electrons and holes following photoexcitation. We modeled our charge transfer state by populating the conduction band with electrons either at 1.55 eV (800 nm) or 3.1 eV (400 nm) above the valence band maximum (VBM) and similarly populating the valence band with holes to model the movement of carriers following photoexcitation. This population of electrons and holes effectively forbids or allows XUV transitions to specific points in k-space but does not account for carrier density, therefore, the modeled peak position and relative intensity is used to compare

experiment to theory. We model our transient XUV spectra by subtracting the calculated ground state spectrum from the calculated excited state spectra to calculate the differential absorption. **Figures 3 and 4** in the main text demonstrate agreement between DFT+BSE modeled 400 nm and 800 nm charge transfer states, respectively.

A thermal isotropic expansion of the GdFeO₃ unit cell was modeled to determine if thermal effects were present in the experimental spectra and is described previously.²³ We isotropically expanded the GdFeO₃ unit cell to model temperatures from 293 K up to 500 K.²⁴ The spectrum of a modeled 350 K expansion can be seen in **Figure S4C and D**. We find no significant contributions of thermal isotropic lattice expansion to 800 nm or 400 nm excited transient XUV spectra.

S3.5. Fe M_{2,3} Edge DFT+BSE Polaron State Calculations

Our semi-empirical method for modeling transient effects of photoexcited polaron formation on XUV core-level spectra is achieved using our DFT+BSE framework and has been described previously.²³ Electron polarons are modeled by locally applying an expansion to Fe-O bonds at one iron octahedra in the GdFeO₃ unit cell. Similarly, hole polarons are modeled by applying a local contraction to the Fe-O bonds in an FeO₆ octahedra. **Figure S8** demonstrates the change in intensity between a modeled electron polaron and hole polaron centered on iron. Both polarons were modeled with a 5% isotropic distortion of the local FeO₆ octahedra. The electron polaron has a higher spectral intensity than the hole polaron. We also simultaneously model electron and hole polarons at neighboring iron sites by employing an expansion and contraction to consider spectrally convolved electron and hole polarons at the Fe M_{2,3} edge (**Fig. S8**). The electron and hole polarons on iron centers are spectrally convolved at the Fe M_{2,3} edge, and occur at the same energy alignment, which is shifted to higher energy relative to the charge transfer state. These anisotropic distortions to the GdFeO₃ unit cell are then applied to our DFT+BSE method and the resulting X-ray spectrum is treated similarly to our excited state calculation detailed in **S3.4** to generate a differential absorption spectrum (**Fig. S8**).

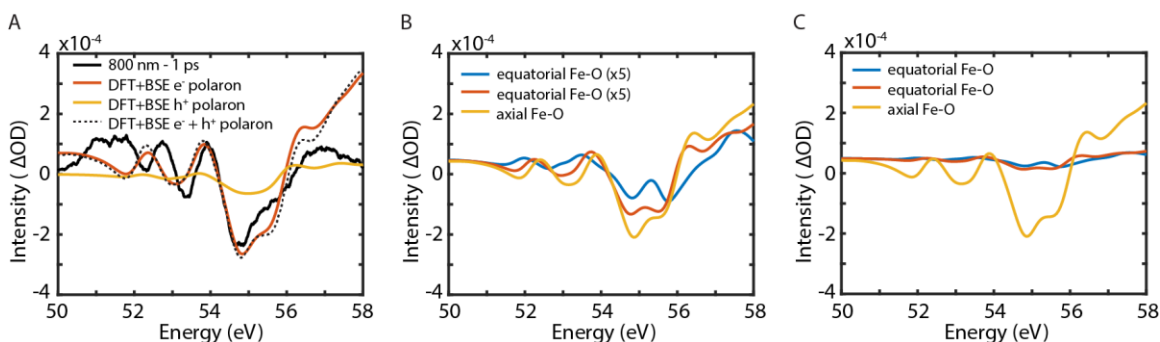


Figure S8. (A) Experimental lineout (black solid) 1 ps after 800 nm photoexcitation compared to DFT+BSE modeled electron (red) and hole (yellow) polarons and compared to a convolved DFT+BSE electron and hole polaron at neighboring iron atoms (black dashed). The DFT+BSE modeled hole polaron is much weaker than the electron polaron due to its delocalized nature, and when convolved together the electron polaron dominates the predicted dynamics. (B) A DFT+BSE modeled electron polaron for an anisotropic expansion of either the equatorial (blue and red) or axial (yellow) Fe-O bonds. The equatorial lineouts are each scaled by 5 times to be compared to the axial distortion. The equatorial ligand expansion is significantly weaker than the axial ligand expansion as plotted in (C) and demonstrates that axial distortions dominate the spectral signature of polaron formation.

Additionally, we model an anisotropic polaronic distortion to stimulate the Jahn-Teller effect. To achieve this distortion, we selectively distort equatorial or axial ligands in the FeO_6 octahedra. **Figure S8B and C** shows that an anisotropic polaronic expansion results in different spectral contributions to the signature of the polaron. We find that axial distortions have a greater effect on the spectral intensity of the polaronic feature in the transient XUV spectrum, which agrees with our findings that the polaronic distortion induces a Jahn-Teller type distortion in the lattice.

S3.6. Fe $M_{2,3}$ Edge pSIC+DFT+BSE Polaron State Calculations

In addition to our semi-empirical modeling of polaronic distortions, we apply the polaronic distortions obtained from the ab initio defect supercell calculations discussed in **S3.2** to our DFT+BSE approach, which we refer to as pSIC+DFT+BSE. The distortion acts as the input for OCEAN and enables us to simulate the excited state X-ray edges that result from the ab initio electron and hole polaron distortions calculated using the defect supercell method.

S4. Ligand-Field Multiplet Theory Calculations

Ligand-field multiplet theory calculations (CTM4XAS) were conducted to model the XUV absorption of oxidation and spin states of different iron species.²⁵ The different oxidation states were modeled by designating the final state of the initial Fe^{3+} state to be either Fe^{2+} or Fe^{4+} . Spin configurations of the photoexcited Fe^{2+} and Fe^{4+} states were modeled by varying the cubic crystal field splitting (10Dq) and the exchange energy (J) for either configuration. The Fe^{3+} high-spin

ground state was subtracted from the Fe^{2+} and Fe^{4+} excited states to generate predicted difference spectra following photoexcitation. **Figure S9** compares these difference spectra with the experimental 400 nm LMCT, 800 nm MMCT, and 800 nm polaron states. The ground state bleach of the Fe^{3+} high-spin feature was shifted to align with experimental bleach at the Fe $M_{2,3}$ edge. The 400 nm LMCT state agrees with a high-spin Fe^{2+} state (**Fig. S9A**) and the 800 nm polaron state (**Fig. S9C**) agrees well with a Fe^{2+} low-spin and Fe^{4+} high-spin configuration.

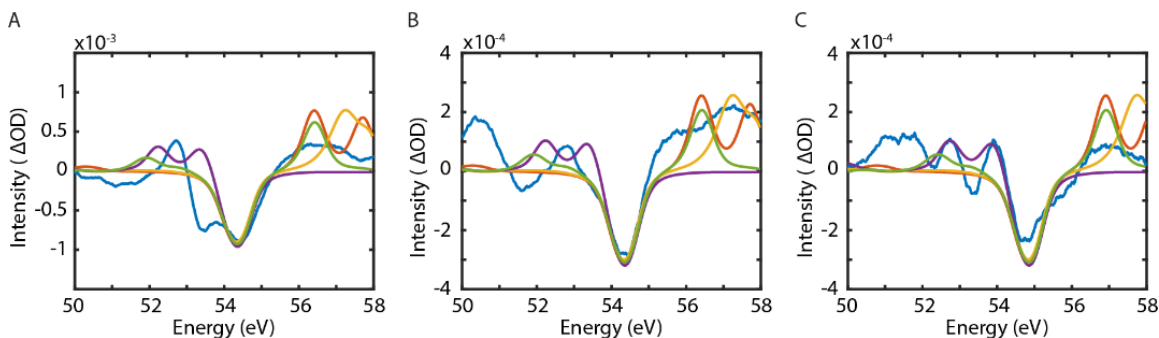


Figure S9. (A) 400 nm LMCT state, (B) 800 nm MMCT state, (C) 800 nm polaron state. Experimental (blue), Fe^{4+} high-spin state (yellow), Fe^{4+} low-spin state (red), Fe^{2+} high-spin state (green), Fe^{2+} low-spin state (purple).

References

1. Makuła, P., Pacia, M. & Macyk, W. How to correctly determine the band gap energy of modified semiconductor photocatalysts based on UV–Vis spectra. *J. Phys. Chem. Lett.* **9**, 6814–6817 (2018).
2. Kim, Y.-J. *et al.* Coherent charge hopping suppresses photoexcited small polarons in ErFeO_3 by antiadiabatic formation mechanism. *Sci. Adv.* **10**, eadk4282 (2024).
3. Liu, H. *et al.* Measuring photoexcited electron and hole dynamics in ZnTe and modeling excited state core-valence effects in transient extreme ultraviolet reflection spectroscopy. *J. Phys. Chem. Lett.* **14**, 2106–2111 (2023).
4. Géneaux, R., Chang, H.-T., Schwartzberg, A. M. & Marroux, H. J. B. Source noise suppression in attosecond transient absorption spectroscopy by edge-pixel referencing. *Opt. Express* **29**, 951–960 (2021).
5. Codling, K., Madden, R. P. & Ederer, D. L. Resonances in the photo-ionization continuum of Ne I (20–150 eV). *Phys. Rev.* **155**, 26–37 (1967).
6. Perdew, J. P., Burke, K. & Ernzerhof, M. Generalized gradient approximation made simple. *Phys. Rev. Lett.* **77**, 3865–3868 (1996).
7. Giannozzi, P. *et al.* QUANTUM ESPRESSO: a modular and open-source software project for quantum simulations of materials. *J. Phys. Condens. Matter* **21**, 395502 (2009).
8. Giannozzi, P. *et al.* Advanced capabilities for materials modelling with Quantum ESPRESSO. *J. Phys. Condens. Matter* **29**, 465901 (2017).
9. Zhu, X.-H., Xiao, X.-B., Chen, X.-R. & Liu, B.-G. Electronic structure, magnetism and optical properties of orthorhombic GdFeO_3 from first principles. *RSC Adv.* **7**, 4054–4061 (2017).
10. Freysoldt, C. *et al.* First-principles calculations for point defects in solids. *Rev. Mod. Phys.* **86**, 253–305 (2014).

11. Kresse, G. & Furthmüller, J. Efficiency of ab-initio total energy calculations for metals and semiconductors using a plane-wave basis set. *Comput. Mater. Sci.* **6**, 15–50 (1996).
12. Heyd, J., Scuseria, G. E. & Ernzerhof, M. Hybrid functionals based on a screened Coulomb potential. *J. Chem. Phys.* **118**, 8207–8215 (2003).
13. Paier, J., Marsman, M., Hummer, K., Kresse, G., Gerber, I. C., Angyan, J. G. Screened hybrid density functionals applied to solids. *J. Chem. Phys.* **124**, 154709 (2006).
14. Sadigh, B., Erhart, P. & Åberg, D. Variational polaron self-interaction-corrected total-energy functional for charge excitations in insulators. *Phys. Rev. B* **92**, 075202 (2015).
15. Zhou, F., Sadigh, B., Erhart, P. & Åberg, D. Ab initio prediction of fast non-equilibrium transport of nascent polarons in SrI₂: a key to high-performance scintillation. *Npj Comput. Mater.* **2**, 1–7 (2016).
16. Kresse, G. & Joubert, D. From ultrasoft pseudopotentials to the projector augmented-wave method. *Phys. Rev. B* **59**, 1758–1775 (1999).
17. Blöchl, P. E. Projector augmented-wave method. *Phys. Rev. B* **50**, 17953–17979 (1994).
18. Ong, S. P. *et al.* Python materials genomics (pymatgen): A robust, open-source python library for materials analysis. *Comput. Mater. Sci.* **68**, 314–319 (2013).
19. Jain, A. *et al.* Commentary: The Materials Project: A materials genome approach to accelerating materials innovation. *APL Mater.* **1**, 011002 (2013).
20. Vinson, J. Advances in the OCEAN-3 spectroscopy package. *Phys. Chem. Chem. Phys.* **24**, 12787–12803 (2022).
21. Gilmore, K. *et al.* Efficient implementation of core-excitation Bethe–Salpeter equation calculations. *Comput. Phys. Commun.* **197**, 109–117 (2015).
22. Vinson, J., Rehr, J. J., Kas, J. J. & Shirley, E. L. Bethe-Salpeter equation calculations of core excitation spectra. *Phys. Rev. B* **83**, 115106 (2011).
23. Klein, I. M., Liu, H., Nimlos, D., Krotz, A. & Cushing, S. K. Ab initio prediction of excited-state and polaron effects in transient XUV measurements of α -Fe₂O₃. *J. Am. Chem. Soc.* **144**, 12834–12841 (2022).
24. Chavan, S. V. & Tyagi, A. K. Nanocrystalline GdFeO₃ via the gel-combustion process. *J. Mater. Res.* **20**, 2654–2659 (2005).
25. Stavitski, E. & de Groot, F. M. F. The CTM4XAS program for EELS and XAS spectral shape analysis of transition metal L edges. *Micron* **41**, 687–694 (2010).